Applied Geochemistry 191 (2025) 106513

Contents lists available at ScienceDirect

Applied Geochemistry

journal homepage: www.elsevier.com/locate/apgeochem

# Aqueous phase stability of multinary thiostannates

Giordano Montegrossi [a,b], Federica Meloni [a,b,c], Andrea Giaccherini [d], Alessandro Veneri [d], Matteo Ardit [e], Matteo Mannini [b,d], Francesco Di Benedetto [f,g,*]

[a] Consiglio Nazionale delle Ricerche, Istituto di Geoscienze e Georisorse, Firenze, Italy
[b] Consorzio Interuniversitario Nazionale di Scienza e Tecnologia dei Materiali (INSTM), Research Unit of Florence, Italy
[c] Dipartimento di Scienze della Terra, Università di Firenze, Firenze, Italy
[d] Dipartimento di Chimica, Università di Firenze, Firenze, Italy
[e] Dipartimento di Geoscienze, Università di Padova, Padova, Italy
[f] Dipartimento di Fisica e Scienze della Terra, Università di Ferrara, Ferrara, Italy
[g] Consorzio Interuniversitario Nazionale di Scienza e Tecnologia dei Materiali (INSTM), Research Unit of Ferrara, Italy

## ARTICLE INFO

Editorial handling by Elisa Sacchi

*Keywords:*
Sulfides
Stability
Pourbaix diagrams
Structural chemistry
Semiconductors for photovoltaics

## ABSTRACT

This research proposes a comprehensive study of the thermodynamic stability of the structurally similar Cu–Fe–Zn–Sn–S multinary sulfides, critical materials that are pivotal in advancing semiconductor technologies. In light of the scarcity of thermodynamic data in the extant literature concerning a relevant number of mineral phases, the missing data were estimated using a method based on the sum of molecular fragments. Consequently, a novel numerical extrapolation method derived from experimental thermochemical stability constants is integrated with the simulation capabilities of the PHREEQC software. This integration facilitates the meticulous charting (using the formalism of Pourbaix diagrams) of the stability domains of Cu–Fe–Zn–Sn–S multinary sulfides in aqueous environments. The present analysis addresses a critical knowledge gap regarding the aqueous stability of multinary sulfides, while introducing a robust theoretical framework for predicting their environmental and technological viability. This objective is accomplished by delineating the relative stability and precipitation boundaries of the studied phases, thereby providing invaluable insights for the development of these sustainable semiconducting materials. Consequently, this research makes two significant contributions. Firstly, it contributes to the theoretical understanding of multinary sulfide systems. Secondly, it establishes the foundation for their practical application in green technologies.

## 1. Introduction

Multinary sulfides have garnered considerable attention in the research community as a potential source of novel semiconducting materials for advanced technological applications. In particular, a number of these technologies are regarded as having considerable potential in the context of the recent decarbonization initiatives undertaken by numerous major economies worldwide. The clearest example of such a strategic role is undoubtedly provided by kesterites (a group of 2nd generation p-type materials for solar energy conversion). It is expected that the use of these materials will contribute to the mitigation of environmental concerns associated with the exploitation of devices grounded on toxic or extremely rare elements (Wang and et al., 2023). Another extensively endorsed application of many materials belonging to this class is in thermoelectrics (Baláž, 2024; Baláž et al., 2021a). Moreover, these materials have been considered for the manifestation of photocatalytic (Olatunde and Onwudiwe, 2022) or metallic conduction (Wu et al., 2007) properties in specific phases.

The considerable interest in multinary sulfides has prompted relevant research, especially in the synthesis of novel materials and the application of the most studied phases in the assembly of innovative devices (Digraskar et al., 2019). Nevertheless, for many of these complex phases, there remains knowledge gap regarding their thermodynamic stability, especially when in contact with aqueous solutions. The present study aims to address this lacuna by providing novel data on the relative stability of the phases. Indeed, the boundaries of their field of existence as solid precipitates in contact with aqueous solutions will be described, thus defining the stability limits of devices containing such materials when in contact with aqueous solutions or moisture. The aim is fulfilled through a strategy that incorporates PHREEQC as a calculation software,

---

* Corresponding author. via Saragat 1, I-44122, Ferrara, Italy.
*E-mail address:* francesco.dibenedetto@unife.it (F. Di Benedetto).

https://doi.org/10.1016/j.apgeochem.2025.106513
Received 2 April 2025; Received in revised form 9 July 2025; Accepted 28 July 2025

the sum of molecular fragments as a method for providing the missing thermodynamic data, and the comparative analysis of the stability diagrams calculated for the various phases in contact with aqueous solutions.

## 2. Calculation of missing thermodynamic constants through the sum of molecular fragment energies

The experimental approach used in the present study to estimate the missing thermodynamic constants of phases belonging to the Cu–Fe–Zn–Sn–S system is grounded on the extrapolation of such quantities as the sum of the thermodynamic constants associated with molecular fragments identified as highly frequent or "characteristics" of the phases belonging to the system. To verify the correctness of this assumption, we have carried out:

1) a systematic review of the structural motifs observed in the Cu–Fe–Zn–Sn–S system, which is systematically presented in section 2.1;
2) the compilation of a database that encompasses all available experimental thermodynamic data on phases belonging to the system; this database is described in section 2.2. Since the final database will be

**Table 1**
List of the phases belonging to the Cu–Fe–Zn–Sn–S system with at least one metal cation and Sn. Their description as minerals (where available), their Me:S ratio and space group symmetry, the occurrence of cation disorder and the valence states of the metals are listed.

| # | Formula unit | Mineral name | Me:S ratio | Packing | Space group | Cation disorder | VS * | reference | | |
|---|---|---|---|---|---|---|---|---|---|---|
| | | | | | | | | mineral | synthetic | calculated |
| 1 | $Cu_4SnS_4$ | – | *>1* | *ccp* | *Pnma* | Y | $Cu^+$,$Sn^{4+}$ | | (Wu et al., 1986; Jaulmes et al., 1977; Choudhury et al., 2017; Wang, 1974) | |
| 2 | $Cu_2SnS_3$ | mohite | | *ccp* | *Cc* | | $Cu^+$,$Sn^{4+}$ | Kovalenker (1983) | (Onoda and et al., 2000; Lohani et al., 2020) | |
| | | | | *ccp* | *F*-43*m* | Y | | | (Lohani et al., 2020; Baláž et al., 2021b) | |
| | | | *1* | *ccp* | *I*-42*m* | Y | | | (Olatunde and Onwudiwe, 2022; Chen and et al., 1998) | |
| | | | | *ccp* | *P*1 | | | | (Wu et al., 1986; Wang, 1974) | |
| | | | | *hcp* | *P*6$_3$*mmc* | | | | | Wu et al. (2007) |
| 3 | $Cu_3SnS_4$ | kuramite | *1* | *ccp* | *I*-42*m* | Y | $Cu^+$,<br>$Cu^{2+}$,<br>$Sn^{4+}$ | Kovalenker (1981) | (Wu et al., 1986; Goto et al., 2013; Zalewski et al., 2010) | |
| 4 | $Cu_5Sn_2S_7$ | – | *1* | | *C*2 | | $Cu^+$,<br>$Cu^{2+}$,<br>$Sn^{4+}$ | | Pavan Kumar et al. (2021) | |
| 5 | $Cu_{11}Sn_5S_{16}$ | – | *1* | *ccp* | *P*-43*n* | Y | $Cu^+$,<br>$Cu^{2+}$,<br>$Sn^{4+}$ | | Kumar et al. (2021) | |
| 6 | $Cu_2Sn_3S_7$ | – | *<1* | | *Cc* | | $Cu^+$,$Sn^{4+}$ | | (Wu et al., 1986; Wang, 1974) | |
| 7 | $Cu_4SnS_6$ | – | *<1* | *hcp* | *R*-3*m* | Y | $Cu^+$,<br>$Cu^{2+}$,<br>$Sn^{4+}$ | | Chen et al. (1999) | |
| 8 | $Cu_4Sn_7S_{16}$ | – | *<1* | *hcp* | *R*-3*m* | | $Cu^+$,$Sn^{4+}$ | | Chen and et al., 1998 | |
| 9 | $Cu_{10}Sn_2S_{13}$ | – | <1 | *ccp* | tetragonal | Y | $Cu^+$,<br>$Cu^{2+}$,<br>$Sn^{4+}$ | | (Wu et al., 1986; Wang, 1976) | |
| 10 | $Cu_6FeSn_2S_8$ | chatkalite | *>1* | *ccp* | *P*-4*m*2 | | $Cu^+$,<br>$Fe^{2+}$,<br>$Sn^{4+}$ | (Mighell, 2006; Fleischer and et al., 1982) | Baláž, 2024 | |
| 11 | $Cu_6Fe_2SnS_8$ | mawsonite | *>1* | *ccp* | *P*-4*m*2 | | $Cu^+$,<br>$Fe^{3+}$,<br>$Sn^{4+}$ | (Mighell, 2006; Szymanski, 1976; Markham and Lawrence, 1965; Yamanaka and Kato, 1976) | Baláž et al. (2019) | Siloi et al. (2019) |
| 12 | $Cu_8(Fe,Zn)_3Sn_2S_{12}$ | stannoidite | *>1* | *ccp* | *I*222 | | $Cu^{+/2+}$,<br>$Fe^{2+}$,<br>$Zn^{2+}$,<br>$Sn^{4+}$ | (Kudoh and Takeuchi, 1976; Yamanaka and Kato, 1976) | (Baláž et al., 2017a, 2021a; Yamanaka and Kato, 1976; Pavan Kumar et al., 2017) | |
| 13 | $Cu_2FeSnS_4$ | stannite | *1* | *ccp* | *I*-42*m* | | $Cu^+$,<br>$Fe^{2+}$,<br>$Sn^{4+}$ | Bonazzi (2003) | (Baláž et al., 2017a, 2017b, 2019, 2021a; Meng, 2015) | |
| 14 | $Cu_2ZnSnS_4$ | kesterite | *1* | *ccp* | *I*-42*m* | Y | $Cu^+$,<br>$Zn^{2+}$,<br>$Sn^{4+}$ | (Bonazzi, 2003; Schorr et al., 2007) | Baláž et al. (2021b) | |
| 15 | $(Cu,Fe)_3SnS_4$ | petrukite | *1* | *ccp* | *Pmn*2$_1$ | Y | $Cu^{+/2+}$,<br>$Fe^{2+}$,<br>$Sn^{4+}$ | Kissin and Owens (1989) | Olatunde and Onwudiwe (2022) | |
| 16 | $Cu_2FeSn_3S_8$ | rhodostannite | *<1* | *ccp* | *I*4$_1$/*a* | Y | $Cu^+$,<br>$Fe^{2+}$,<br>$Sn^{4+}$ | Springer (1968) | (Baláž et al., 2017a, 2017b, 2021a, 2021b; Meng, 2015; Jumas et al., 1979) | |

VS – Valence state, as defined in the cited reference(s).

used to calculate the aqueous stability of the investigated phases, it has been developed in the framework of the existing general-purpose geochemical databases compatible with the PHREEQC code.

### 2.1. Chemical and structural trends of phases belonging to the Cu–Fe–Zn–Sn–S system

We focused our effort on a selected set of thiostannates accordingly to the literature definition (Moëlo et al., 2008), i.e. the phases explicitly containing Sn and at least one other metal cation among Cu, Fe and Zn (see Table 1), while neglecting other phases belonging to the simpler subsystems (*e.g.*, Cu–S, Cu–Fe–S, Sn–S, …) which description can be found in earlier reports (Aquino, 2020; Giaccherini et al., 2016; Huang, 2016).

#### 2.1.1. Chemical trends

The classification of sulfide minerals can be facilitated by considering the ratio of metal to sulfur, which is mainly 1:1 for the compounds reported in Table 1 (*e.g.*, Dana's mineral classification (webmineral.com, 2024)). Exceptions include metal-rich phases ($Cu_4SnS_4$, chatkalite, $Cu_6FeSn_2S_8$; mawsonite, $Cu_6Fe_2SnS_8$ and stannoidite $Cu_8(Fe,Zn)_3Sn_2S_{12}$) and sulfur-rich phases ($Cu_2Sn_3S_7$, $Cu_4Sn_7S_{16}$, $Cu_{10}Sn_2S_{13}$, and rhodostannite, $Cu_2FeSn_3S_8$). All phases in Table 1 can be plotted in the tetrahedral diagram of Fig. 1. The #1 - #9 phases (Giaccherini et al., 2016; Wu et al., 1986) properly belong to the ternary Cu–Sn–S diagram and lie on one of the faces of the tetrahedron. With regard to the phases belonging to the quinary Cu–Fe–Zn–Sn–S system, an interesting way of presenting the chemical relationship between these sulfides is to consider the formal valence of the metal cations: most of the phases have only Cu(I), Fe(II) (or Zn(II)) and Sn(IV), respectively. In all phases of Table 1 except $Cu_4SnS_6$ (Chen et al., 1999), the presence of sulfur is either experimentally verified or at least assumed to be present only in its divalent reduced state S(-II). Indeed, suitable ternary subfields can be identified to describe the chemical variability of the phases within the tetrahedral diagram (colored regions of Fig. 1). The details of the ternary/pseudoternary field depicted in Fig. 1 are elucidated in the Supporting Information, Figures SI1- SI4.

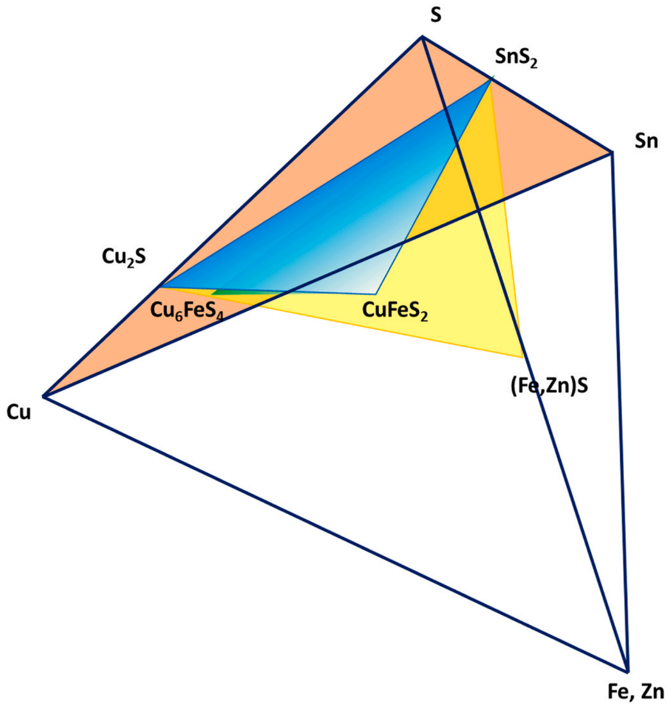

**Fig. 1.** Four component tetrahedral Cu, (Fe,Zn), Sn, S phase system showing four ternary/pseudoternary fields relevant to classify the phases considered in the study: Cu–Sn–S (orange field); $Cu_2S$-(Fe,Zn)S–$SnS_2$ (yellow field); $Cu_2S$–$CuFeS_2$–$SnS_2$ (blue field); $Cu_6FeS_4$–$CuFeS_2$–$SnS_2$ (green field). Details of the four ternary/pseudoternary fields are given in the Supporting Information file.

#### 2.1.2. Structural trends - phases with Me:S ratio = 1

The main thiostannates of the systems under consideration are all based on a tetrahedral coordination of the metal cations and a cubic or hexagonal close-packed (*ccp* and *hcp*) distribution of the S anions. The archetypal structural models are those of the *ccp* and *hcp* ZnS polymorphs: sphalerite, cubic with space group (SG) $F\bar{4}3m$, and wurtzite, hexagonal with SG $P6_3mc$ (Kissin and Owens, 1989; Schorr, 2007). In both structural models, Zn cations occupy half of the available tetrahedral cavities.

These two archetypes are structural reference for all minerals and phases in Table 1 with a unitary ratio between the sum of the metal cations and anions: *ccp* (for stannite, kuramite, kesterite and $Cu_{11}Sn_5S_{16}$) and *hcp* (for petrukite and $Cu_5Sn_2S_7$) (Fig. 2a and b).

A relevant feature of all these structures is the pattern that emerges from the distribution of cations in the tetrahedral voids, resulting in a decrease of symmetry (Table 1). Some phases (namely stannite, mohite and $Cu_5Sn_2S_7$) exhibit a complete ordering of metal cations, whereas some others (kesterite, kuramite, petrukite and $Cu_{11}Sn_5S_{16}$) show sites with mixed metal occupancies in their structural models (Kovalenker, 1981; Bonazzi, 2003; Schorr et al., 2007; Kumar et al., 2021; Pavan Kumar et al., 2021). Examples of these two classes are shown in Fig. 2c and d. It is worth noting that, despite the limited X-rays resolution with respect to the isoelectronic cations Cu(I) and Zn(II) and a different cationic pattern (Kissin and Owens, 1989; Hall et al., 1978), it has been proposed that the crystal structure of kesterite could be indexed in the SG $I\bar{4}$. In this study, the structural solution by neutron diffraction data is used (Schorr et al., 2007). Another peculiar case is that of mohite, a phase whose structure has been described in at least three different arrangements as a function of an assumed cation disorder in the tetrahedral cavities (Onoda and et al., 2000; Lohani et al., 2020; Chen and et al., 1998). A complete set of the relevant patterns of all the phases here considered is shown in the Supporting Information, Figures SI5-SI11.

#### 2.1.3. Phases with Me/S ratio >1

When the chemistry of the mineral determines chemical ratios that deviate from the 1:1 Me/S ratio (Table 1), the challenge of finding a suitable crystallographic site within the structure to accommodate the excess metal cations arises. As only half of the available tetrahedral sites are occupied by metal cations in the sphalerite/wurtzite structures, mawsonite and chatkalite exhibit an extra occupied tetrahedral void (Fig. SI7a). This feature gives rise to ribbons of edge-sharing tetrahedral Fe sites, shown in Fig. 3a, which run parallel to one of the three crystallographic axes.

In mawsonite, the additional tetrahedral void hosts an Fe ion. In this phase, Fe occurs in two non-equivalent positions: the first (1*b* in Wyckoff notation) is the regular site of the stannite-type tetrahedral arrangement and the second (1*c*) is the extra site. In chatkalite, which is structurally close to mawsonite (Baláž, 2024; Mighell, 2006; Fleischer and et al., 1982), the $Fe_2^{3+}Sn^{4+}$ group is replaced by an isoelectronic $Fe^{2+}Sn_2^{4+}$ group (Mighell, 2006). Replacing Fe with Sn at site 1*c* would result in a tetrahedron with six edge-sharing tetrahedral next-neighbors (Fig. SI7a-b). Conversely, replacing Fe with Sn at site 1*b* would result in only two edge-sharing neighbors. In this study, it is assumed that Sn may be replacing Fe at site 1*b*. However, the potential for alternative arrangements involving Cu ions in the replacement mechanisms cannot be ruled out. According to the chosen configuration, the extra void is occupied by Fe also in chatkalite.

The mineral stannoidite explains its stoichiometry through the use of a structural solution analogous to that observed in the cases of chatkalite

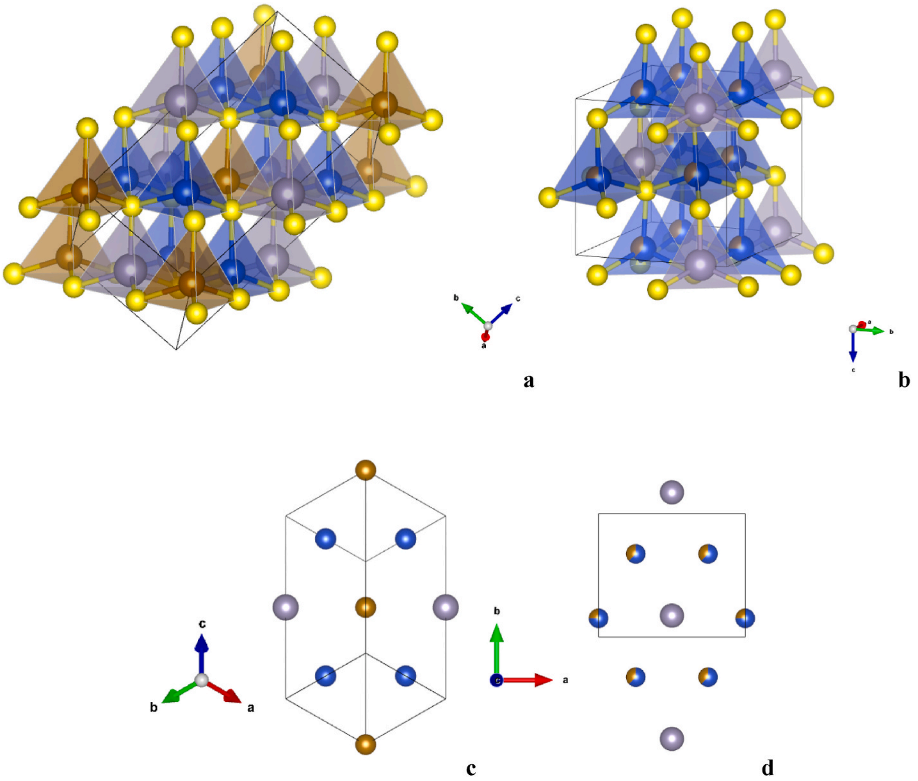

**Fig. 2.** Structural models of (a) stannite and (b) petrukite viewed along [212] and [2$\bar{1}$0], respectively (*i.e.*, oriented so that the tetrahedra are aligned with one corner up). Stannite and petrukite exhibit models derivative of those of sphalerite and wurtzite, respectively. Simplified view of the structural details highlighting the cation patterns in the models of: (c) stannite, along [112], and (d) petrukite along [001]. Structures are tilted to give a comparable view of a plane of tetrahedral void. Stannite and petrukite are example of absence and presence of partially disordered site occupancies, respectively. Colour code: S (yellow), Cu (blue), Sn (grey), Fe (brown). Structural models are realized using the Vesta 4.6.0 software (Momma and Izumi, 2011).

and mawsonite, wherein an extra tetrahedral cavity is occupied (Kudoh and Takeuchi, 1976). The resulting structural model is shown in Figure SI7c. Again, the Me/S $>$ 1 condition is solved by an extra tetrahedral site, which is occupied by a Cu ion in this case. This results in the formation of ribbons of tetrahedral Cu sites parallel to the *b*-axis direction (Fig. 3b). Simplified views of the three minerals, emphasizing the patterns of metal sites, are shown in Figure SI8.

Another phase with excess metal cations is $Cu_4SnS_4$, in which the excess Cu ions are accommodated by filling part of the empty octahedral voids (Fig. SI9) (Jaulmes et al., 1977; Choudhury et al., 2017) in a 3-fold almost planar coordination. This structural motif is somewhat similar to that in the $Cu_{2-x}S$ minerals (Evans, 1979).

### 2.1.4. Phases with Me/S ratio $<$1

When the number of cations in the structure is smaller than the number of sulfide anions, a spinel-like structural arrangement (Fig. SI10) is observed in rhodostannite (Skinner et al., 1964), and in synthetic $Cu_4Sn_7S_{16}$, CTS (Chen and et al., 1998). Rhodostannite, like greigite, exhibits a Me/S ratio that is equivalent to that of thiospinels (Skinner et al., 1964). It has been identified that a topological relationship joins the structural model of rhodostannite and thiospinel. In rhodostannite, the specificity of the cation distribution within the sites results in a tetragonal symmetry. With the exception of the different Me/S ratio (0.75 in rhodostannite and thiospinel, 0.6875 in CTS), the main difference between the two structures pertains to the occupancy of the octahedral voids, with a random distribution of Fe and Sn in rhodostannite and an ordered distribution of Cu and Sn in CTS (Fig. 3c and d). Conversely, the crystal structure of $Cu_4SnS_6$ (Fig. SI11) (Chen et al., 1999), another phase with Me:S $<$ 1 ratio, shows similarities with the layered structure of covellite (Ohmasa et al., 1977), and $ZnIn_2S_4$. (Chong and et al., 2022). However, tetrahedral, octahedral and/or triangular cationic sites have been observed to coexist with the disulfide anions, resulting in an unconventional charge balance and distinctive electric properties (Chen et al., 1999; Di Benedetto et al., 2006).

## 2.2. The thermochemical database: state of the art

The geochemical code PHREEQC (v. 3.5.0) was used to estimate the aqueous phase equilibria of the minerals (Parkhurst and Appelo, 1999). This code calculates the equilibria between aqueous solutions and minerals, gases, solid solutions, exchangers and sorption surfaces, implementing several types of aqueous activity models. The results of the PHREEQC calculation critically depend on the database used. Most databases use the Davies equation (B-Dot activity model) (Helgeson and et al., 1978, 1981) such as the Lawrence Livermore National Laboratory (LLNL) model (Delany and Lundeen, 1991), minteq.v4 (Allison et al., 1991), Thermoddem (Blanc et al., 2012), and Soltherm (University of Oregon, 2015). The available literature thermochemical data for some sulfide minerals can already be found in some widely used databases (Blanc et al., 2012; University of Oregon, 2015; Johnson et al., 1992). In particular, experimental thermochemical constants have been obtained for the phases listed in Table 2. We operated on the soltherm database, integrated with items from the LLNL database as already indicated by (Giaccherini et al., 2016). Unfortunately, none of the phases listed in Table 1 are included in the list. For the sake of completeness, in a previous study by our group, the thermochemical constants of the mohite and kuramite phases were calculated by extrapolation from the data of other phases available in the literature (Giaccherini et al., 2016). Similarly, specific studies reporting calculated thermochemical constants for stannite, kesterite and mawsonite can be found in the literature (Siloi et al., 2019; Stolyarova et al., 2018, 2019).

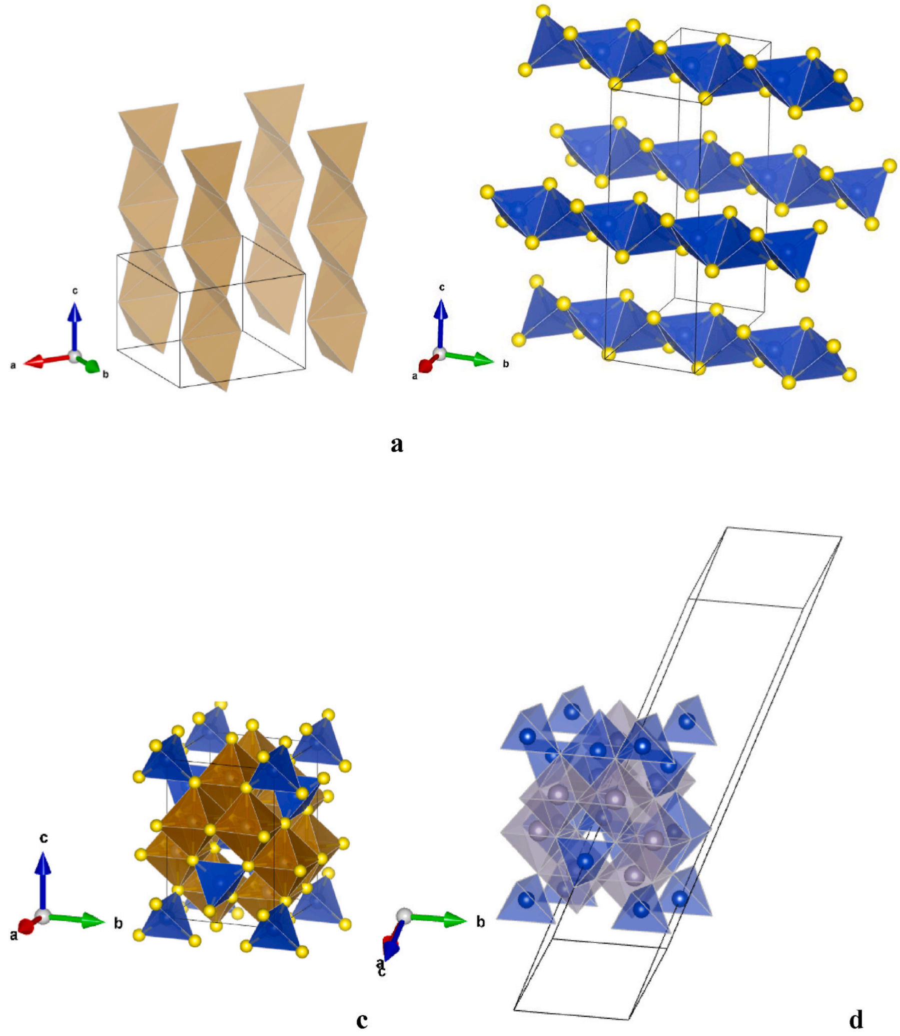

**Fig. 3.** (a) detail of the ribbons of tetrahedral Fe sites parallel to the *c*-axis in the crystal structure of mawsonite viewed along [311]; (b) detail of the ribbons of Cu tetrahedral sites parallel to the *b*-axis in the crystal structure of stannoidite viewed along [210]. (c) rhodostannite along [110] and (d) $Cu_4Sn_7S_{16}$ along [$\overline{2}$ 1 10]. Color code: S (yellow), Cu (blue), Sn (grey), Fe (brown). Structural models are realized using the Vesta 4.6.0 software.

## 3. Results and discussion

### 3.1. *Thermodynamic constants of the newly calculated phases*

From the survey of the chemical trends and structural motifs presented in the previous sections, some general considerations can be extrapolated:

- ✓ Most of the phases host variable amounts of a small group of cations: $Cu^{+}$, $Cu^{2+}$, $Sn^{4+}$ and $Fe^{2+}$. Exceptions are kesterite, where $Zn^{2+}$ is also present, and mawsonite and stannoidite, where $Fe^{3+}$ is apparently revealed by Mössbauer Spectroscopy; (Baláž, 2024; Szymanski, 1976).
- ✓ Most of the structural models consist of a 3D network of tetrahedral sites populated in an ordered (or disordered) way by the different metal cations.

Both considerations suggest that one way of populating the thermochemical database for the phases in Table 1 could be to set up calculated values obtained by linear combination of "molecular" fragments obtainable from some phases in Table 2. From a chemical point of view, formal chemical/redox reactions can be defined as, *e.g.*:

$$Cu_2S + CuS + SnS_2 \rightarrow Cu_3SnS_4 \qquad 1)$$

After which one can define:

$$log\ K_{eq\,Cu_3SnS_4} = \sum\nolimits_{i=Cu_2S,CuS,SnS_2} log\ K_{eq\,i} \qquad 2)$$

The additivity of the terms in the proposed equation (2)) closely resembles that assumed in the Born-Haber cycles, which are based on the first principle of thermodynamics (Kondepudi et al., 1998). In these cycles, the additive property of the formation enthalpies of simple and complex compounds is exploited. In the present case, the use of the $logK_{eq}$ signifies a consideration of analogues additive behavior with respect to the Gibbs energy, to which the $logK_{eq}$ is linked, in accordance with the Van't Hoff isotherm:

$$log\ K_{eq} = -\ \Delta G/_{RT} \qquad 3)$$

The verification of the additivity of the entropy term is a complex process. The application of a method based on the overall additivity of the Gibbs free energy has been documented in literature (Tardy, 1976; Tardy and Garrels, 1974; Tardy and Vieillard, 1977). This method is applied in the extrapolation of thermodynamic data for complex compounds (*e.g.* oxides, layered silicates, phosphates) using a molecular fragment approach.

Here, as an example, an entropy value was calculated through an *ab-initio* approach. This value was then compared with that obtained through estimation from the molar entropies of known compounds

**Table 2**

Thermochemical constants of some sulfide minerals as reported in the literature. The data are expressed as $\log K_{eq}$.

| Phase | soltherm (Johnson et al., 1992) | thermodden (Blanc et al., 2012) | ref (Giaccherini et al., 2016) | ref (Siloi et al., 2019) | ref (Stolyarova et al., 2018) | ref (Stolyarova et al., 2019) | Dissolution reaction |
|---|---|---|---|---|---|---|---|
| covellite, CuS | −24.735 | −22.06 | | | | | $CuS + H^+ = Cu^{2+} + HS^-$ |
| chalcocite, $Cu_2S$ | −35.241 | −30.02 | | | | | $Cu_2S + H^+ = 2Cu^+ + HS^-$ |
| sphalerite, ZnS | −11.44 | −11.145 | | | | | $ZnS+ H^+= Zn^{2+} + HS^-$ |
| herzenbergite, SnS | −15.5786 | | | | | | $SnS + 2H_2O{=\!=}Sn(OH)_2^+ H^+ +2HS^-$ |
| berndtite, $SnS_2$ | −33.271 | −32.151 | | | | | $SnS_2 + 6H_2O{=\!=}Sn(OH)_6^{-2} + 4H^+ + 2HS^-$ |
| ottemannite, $Sn_2S_3$ | −46.268 | | | | | | $Sn_2S_3 +12H_2O = 2Sn\ (OH)_6^{2-} + 2e^- +9H^+ +3HS^-$ |
| $Sn_3S_4$ | −61.98 | | | | | | $Sn_3S_4+18\ H_2O = 3Sn\ (OH)_6^{2-}+ 4e^- +14H^+ +3HS^-$ |
| troilite, FeS | −4.008 | −3.874 | | | | | $FeS + H^+ = Fe^{+2} + HS^-$ |
| mackinawite, FeS | | −3.54 | −4.64 | | | | $FeS + H^+ = Fe^{+2} + HS^-$ |
| pyrite, $FeS_2$ | −24.654 | −23.59 | | | | | $FeS_2 + 2H^+ + 2e^- = Fe^{+2} + 2HS^-$ |
| marcasite, $FeS_2$ | | −22.862 | | | | | $FeS_2 + 2H^+ + 2e^- = Fe^{+2} + 2HS^-$ |
| greigite, $Fe_3S_4$ | | −21.889 | −45.035 | | | | $Fe_3S_4 + 4H^+ = 2Fe^{+3} + Fe^{+2} + 4HS^-$ |
| chalcopyrite, $CuFeS_2$ | −34.045 | | | | | | $CuFeS_2 + 6H_2O = 3\ Cu^{2+}+ Sn\ (OH)_6^{2-}+ 2e^- +2H^+ +4HS^-$ |
| bornite, $Cu_5FeS_4$ | −109.503 | | | | | | $Cu_5FeS_4 + 4H^+ = 5Cu^{+2} + Fe^{+2} + 4e^- + 4HS^-$ |
| mohite, $Cu_2SnS_3$ | | | −58.03 | | | | $Cu_2SnS_3 + 6H_2O = 2Cu^{+2} + Sn\ (OH)_6^{-2} + 3H^+ + 2e^- + 3HS^-$ |
| kuramite, $Cu_3SnS_4$ | | | −73.14 | | | | $Cu_3SnS_4 + 6H_2O = 3Cu^{+2} + Sn\ (OH)_6^{-2} + 2H^+ + 2e^- + 4HS^-$ |
| mawsonite, $Cu_6Fe_2SnS_8$ | | | | −171.88[a] | | | $Cu_6Fe_2SnS_8 + 8H_2O = 6Cu^{+2} + 2Fe^{+2} + Sn(OH)_6^{-2} + 2OH^- + 4e^- + 8HS^-$ |
| stannite, $Cu_2FeSnS_4$ | | | | | −75.50[b] | | $Cu_2FeSnS_4 + 6H_2O = 2Cu^{+2} + Fe^{+2} + Sn(OH)_6^{-2} + 2H^+ + 2e^- + 4HS^-$ |
| kesterite, $Cu_2ZnSnS_4$ | | | | | | −76.51[c] | $Cu_2ZnSnS_4 + 6H_2O = 2Cu^{+2} + Zn^{+2} + Sn(OH)_6^{-2} + 2H^+ + 2e^- + 4HS^-$ |

[a] Calculated from the $E_f$ value, −1.0456486 Ry.

[b] Calculated from the $\Delta H^\circ_f$ value, 419.11 kJ/mol.

[c] Calculated from the $\Delta H^\circ_f$ value, 467.62 kJ/mol.

provided in the comprehensive database by Robie and Hemingway (1995). In order to perform the aforementioned calculation, the vibrational frequencies and elastic constants calculated for kesterite $Cu_2ZnSnS_4$ by Gürel et al. (2011) through an ab-initio DFPT-LDA study were considered. The resulting entropic contribution, as computed by first principles method as reported by Belmonte et al. (2014, 2016 and 2022), yielded a value of $S^0_{vib}$ at $T = 298.15$ and $P = 1$ bar of −71.7 kJ/mol. According to the molecular fragments approach, kesterite can be formally obtained by

$$Cu_2S + ZnS + SnS_2 \rightarrow Cu_2ZnSnS_4 \qquad 4)$$

The sum of the $S^0$ values obtained from the cited database (Robie and Hemingway, 1995) yields −78.2 kJ/mol. The result of this comparison reveals that the difference between the values obtained by the two approaches, i.e., $\Delta S^0_{vib} = 6.5$ kJ/mol, is within the 10 % of the average entropy value. Accordingly, we have demonstrated, at least for kesterite, that the entropy term is additive within the error margin of our established protocol, as will be discussed in greater detail subsequently. The reasonable assumption that the entropy term of the Gibbs free energy also exhibits an additive behavior in the proposed molecular fragment approach extends the validity of the approach to the $\log K_{eq}$ values.

To perform the choice of the best molecular fragment in the calculation, one should consider only those compounds in which the metal cations, in addition to having the correct valence state, should be in a tetrahedral arrangement, in order to take the local structural motif of the target compound into account. Unfortunately, this condition is verified only for $Zn^{2+}$ in sphalerite and for the pair $Cu^+ + Fe^{3+}$ in chalcopyrite. We have carried out a test, as suggested in the literature (Blanc, 2008; Subramani and et al., 2020), by plotting $\log K/x_{Me}$ (*i.e.*, $\log K$ scaled by the molar fraction of metal Me) against the sulfur-to-metal ratio, S/Me, which shows good linearity for all pure metals and binary sulfides of Cu, Fe and Sn (Fig. SI12). Indeed, the difference between the values of the $\log K_{eq}$ for sulfides of the same cation in the same valence state (but different coordination number) gives rise to an uncertainty (accepted here as intrinsic to the linear fitting procedure described and to the thermodynamic data) of the order of 5 % ($R^2$ is 0.94 for Cu, 0.98 for Fe, 0.98 for Sn) of the total $\log K_{eq}$ for a given phase. Accordingly, a minimal set of phases has been selected to extrapolate the thermochemical constants of all the phases listed in Table 1. These phases are chalcocite (for $Cu^+$), covellite ($Cu^{2+}$), mackinawite ($Fe^{2+}$), berndtite ($Sn^{4+}$) and chalcopyrite ($Cu^+$ and $Fe^{3+}$ when present simultaneously in the target phase). As previously stated, the reference phases have been chosen so as to represent the correct valence and coordination number, when possible, and only the valence, when the local coordination is not tetrahedral (e.g chalcocite, covellite, berndtite). In particular, the simplest binary phases were chosen for this second case.

Table 3 shows all phases with the formal equations used to calculate their $\log K_{eq}$ and the final calculated values.

### 3.1.1. Reliability of results

A certain number of phases present in both Tables 2 and 3 were used to perform a consistency test of the calculated values with respect to the experimental values. The result of such a test is shown in Figure SI12. A good linear correlation is obtained between the experimental and calculated $\log K_{eq}$ values. Statistical considerations obtained by the linear regression procedure allowed obtaining slope and intercept

**Table 3**

List of the phases for which the log Keq was calculated according to the procedure described in the text.

| # | Phase | Formal reaction | Log Keq | Dissolution reaction |
|---|---|---|---|---|
| ***1*** | $Cu_4SnS_4$ | $2Cu_2S + SnS_2$ | −103.753 | $Cu_4SnS_4 + 6H_2O = 4Cu^{+2} + Sn(OH)_6^{-2} + 2H^+ + 4e^- + 4HS^-$ |
| ***2–6*** | mohite, $Cu_2SnS_3$ | $Cu_2S + SnS_2$ | −68.512 | $Cu_2SnS_3 + 6H_2O = 2Cu^{+2} + Sn(OH)_6^{-2} + 3H^+ + 2e^- + 3HS^-$ |
| ***7*** | kuramite, $Cu_3SnS_4$ | $Cu_2S + CuS + SnS_2$ | −93.247 | $Cu_3SnS_4 + 6H_2O = 3Cu^{+2} + Sn(OH)_6^{-2} + 2H^+ + 2e^- + 4HS^-$ |
| ***8*** | $Cu_5Sn_2S_7$ | $2Cu_2S + CuS + 2SnS_2$ | −161.759 | $Cu_5Sn_2S_7 + 12H_2O = 5Cu^{+2} + 2Sn(OH)_6^{-2} + 5H^+ + 4e^- + 7HS^-$ |
| ***9*** | $Cu_{11}Sn_5S_{16}$ | $5Cu_2S + CuS + 5SnS_2$ | −367.295 | $Cu_{11}Sn_5S_{16} + 30H_2O = 11Cu^{+2} + 5Sn(OH)_6^{-2} + 14H^+ + 10e^- + 16HS^-$ |
| ***10*** | $Cu_2Sn_3S_7$ | $Cu_2S + 3SnS_2$ | −135.054 | $Cu_2Sn_3S_7 + 18H_2O = 2Cu^{+2} + 3Sn(OH)_6^{-2} + 11H^+ + 2e^- + 7HS^-$ |
| ***11*** | $Cu_4SnS_6$ | $4CuS + SnS_2$ | −132.211 | $Cu_4SnS_6 + 6H_2O = 4Cu^{+2} + Sn(OH)_6^{-2} + 6HS^-$ |
| ***12*** | $Cu_4Sn_7S_{16}$ | $2Cu_2S + 7SnS_2$ | −303.379 | $Cu_4Sn_7S_{16} + 42H_2O = 4Cu^{+2} + 7Sn(OH)_6^{-2} + 26H^+ + 4e^- + 16HS^-$ |
| ***13*** | $Cu_{10}Sn_2S_{13}$ | $Cu_2S + 8CuS + 2SnS_2$ | −299.663 | $Cu_{10}Sn_2S_{13} + 12H_2O + H^+ = 10Cu^{+2} + 2Sn(OH)_6^{-2} + 2e^- + 13HS^-$ |
| ***14*** | chatkalite, $Cu_6FeSn_2S_8$ | $3Cu_2S + FeS + 2SnS_2$ | −176.913 | $Cu_6FeSn_2S_8 + 12H_2O = 6Cu^{+2} + Fe^{+2} + 2Sn(OH)_6^{-2} + 4H^+ + 6e^- + 8HS^-$ |
| ***15*** | mawsonite, $Cu_6Fe_2SnS_8$ | $2Cu_2S + 2CuFeS_2 + SnS_2$ | −188.677 | $Cu_6Fe_2SnS_8 + 8H_2O = 6Cu^{+2} + 2Fe^{+2} + Sn(OH)_6^{-2} + 2OH^- + 4e^- + 8HS^-$ |
| ***16*** | stannoidite, $Cu_8(Fe, Zn)_3Sn_2S_{12}$ | $3Cu_2S + 2CuS + 3FeS + 2SnS_2$ | −252.541 | $Cu_8Fe_3Sn_2S_{12} + 12H_2O = 8Cu^{+2} + 3Fe^{+2} + 2Sn(OH)_6\text{-}^{2+}6e^- + 12HS^-$ |
| ***17*** | stannite, $Cu_2FeSnS_4$ | $Cu_2S + FeS + SnS_2$ | −73.16 | $Cu_2FeSnS_4 + 6H_2O = 2Cu^{+2} + Fe^{+2} + Sn(OH)_6^{-2} + 2H^+ + 2e^- + 4HS^-$ |
| ***18*** | kesterite, $Cu_2ZnSnS_4$ | $Cu_2S + ZnS + SnS_2$ | −79.952 | $Cu_2ZnSnS_4 + 6H_2O = 2Cu^{+2} + Zn^{+2} + Sn(OH)_6^{-2} + 2H^+ + 2e^- + 4HS^-$ |
| ***19*** | petrukite, $(Cu, Fe)_3SnS_4$ | $Cu_2S + FeS + SnS_2$ | −73.16 | $(Cu,Fe)_3SnS_4 + 6H_2O = 2Cu^{+2} + Fe^{+2} + Sn(OH)_6^{-2} + 2H^+ + 2e^- + 4HS^-$ |
| ***20*** | rhodostannite, $Cu_2FeSn_3S_8$ | $Cu_2S + FeS + 3SnS_2$ | −86.625 | $Cu_2FeSn_3S_8 + 18H_2O = 2Cu^{+2} + Fe^{+2} + 3Sn(OH)_6^{-2} + 10H^+ + 2e^- + 8HS^-$ |

parameters close to the ideal values of 1 and 0, respectively, and an overall Pearson $r^2$ parameter of 0.92. This last consideration led to define a value of uncertainty of 10 % for the whole calculation procedure. The linear relationship shown by Figure SI12 can be considered a further confirmation of the validity of the additive assumption for the $\log K_{eq}$ data, at least in the present case.

### 3.1.2. The configurational entropy contribution

We have also investigated the possible role of configurational entropy and found it to be almost negligible in most cases. The entropy contribution in these systems is not only related to the phase formation, but the vibrational, electronic and configurational entropies should also be considered. Indeed, the phases listed in Table 1 suggest the occurrence of phenomena of cation disorder among several crystallographically non-equivalent sites in the structure. Except for all phases for which experimental thermochemical properties are described in the literature (Table 2), the determination of the configurational entropy contribution is relevant in the case of phases with almost identical chemical composition and overall metal coordination, but different cation distribution (see *e.g.* stannite and petrukite) (Table 3). Configurational entropy has been conventionally calculated by considering the probability that a configuration must exist, given by the two equations:

$$W_n^r = \frac{n!}{r_1! r_2! \dots r_k!}$$

and

$$S = RZ\ln W_n^r$$

In these equations, $n$ represents the number of crystallographically non-equivalent sites, and $r_k$ the multiplicity of the $k^{th}$ metal cation involved in the disordered distribution. The exemplary case is indeed that of petrukite. For this mineral the configurational entropy contribution (TS at room temperature) is 5.44 kJ $mol^{-1}$, a value corresponding to ~7.5 % of the ΔG contribution. Thus, the configurational entropy contribution seems to be of little relevance compared to the ΔG (see previous section). In fact, considering that the configurational entropy contribution never exceeds 10 % of the total energy associated with the mineral phase, we have decided to neglect this contribution for all phases except those where this contribution could represent the only difference in energetics (i.e. in the case of stannite/petrukite).

### 3.2. Phase stability by pe-pH diagrams

Using the approach described in the previous section, Fig. 4 shows the pe versus pH stability diagrams for some relevant ternary and multinary mineral phases, respectively. In these contour diagrams, calculated at room temperature, the colored region marks the pe and pH values at which the Saturation Index, SI, is ≥ 0. Remarkably, for all the phases considered in Fig. 4, this is the first description of the stability field to the best of the authors' knowledge. Since we have obtained the thermodynamic constants assuming a given uncertainty, we also evaluated the effects of this uncertainty in the definition of the solubility boundary of some relevant phases in the system. The results of the evaluation are shown and commented in the Supporting Information (Fig. SI13).

Regarding the ternary Cu–Sn–S phases (Fig. 4a–f), it can be observed that the stability fields for $Cu_4SnS_4$, $Cu_4SnS_6$ and $Cu_{12}Sn_4S_{13}$ are limited by the oxidation of the anionic species (S) at high pe, by the reduction of the water hydrogen at low pe and by the formation of complexes of the metal(s) with sulfide and polysulfide anions at high pH. This effect is contrary to the expected result (Le Chatelier principle), according to which increasing the concentration of one of the reactants, i.e. sulfur, should increase the stability of the solid product. For $Cu_5Sn_2S_7$ and $Cu_{11}Sn_5S_{16}$, a further limit at low pH is probably due to the decrease in availability of the $S^{2-}$ and $HS^-$ species in solution, a tendency not compensated by the relatively high $K_{eq}$ of the precipitates. In kuramite, the stability field appears to be significantly reduced and the pH window of existence lies between 3 and 6. In terms of decreasing stability, the following series can be established: $Cu_{12}Sn_4S_{13} > Cu_{11}Sn_5S_{16} > Cu_4SnS_6 > Cu_5Sn_2S_7 \sim Cu_4SnS_4 \gg$ kuramite.

Similar considerations can be made for the quaternary Cu–Fe/Zn–Sn–S phases (Fig. 4g–l). Here, stannoidite is the only mineral whose stability field extends towards low pH values, whereas all other phases undergo significant dissolution at low pH, i.e. between 1 and 2, depending on the mineral phase. As far as Fe and Zn speciation is concerned, at low pH the aqueous species of divalent cations are the most relevant species, whereas at high pH a certain competition between hydroxyls and sulfur anions in binding the metal cations coincides with a reduced stability of the solid phases. It is noteworthy that no phase

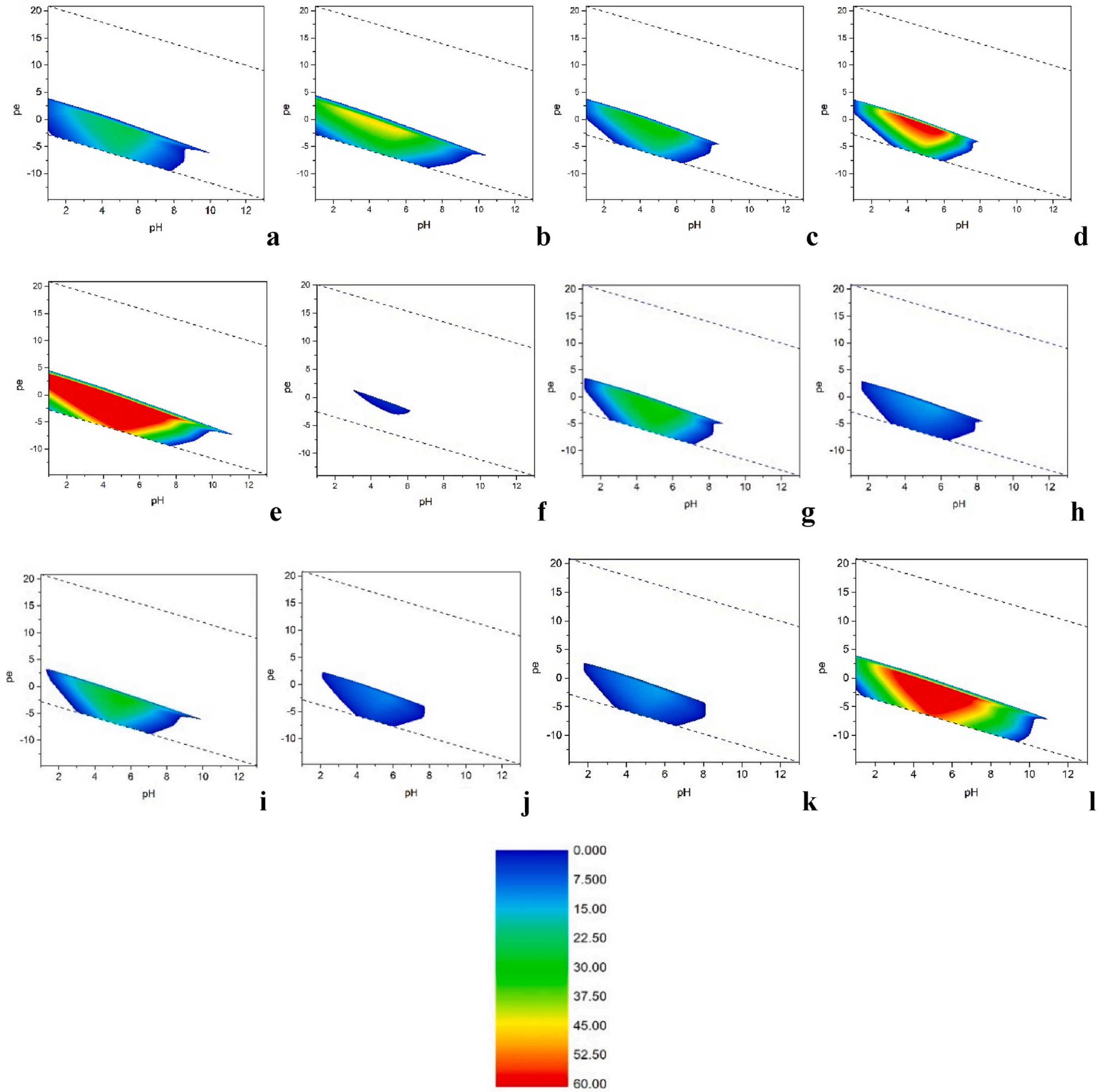

**Fig. 4.** Stability pE-pH diagrams for (a) $Cu_4SnS_4$, (b) $Cu_4SnS_6$, (c) $Cu_5Sn_2S_7$, (d) $Cu_{11}Sn_5S_{16}$, (e) $Cu_{12}Sn_4S_{13}$, (f) kuramite, $Cu_3SnS_4$, (g) chatkalite, (h) kesterite, (i) mawsonite, (j) petrukite, (k) stannite and (l) stannoidite. The calculations were performed at room temperature with the following concentrations: Cu and Sn $1 \cdot 10^{-3}$ mol/Kgw, S $4 \cdot 10^{-3}$ mol/Kgw. The contour plot is obtained by plotting the Saturation Index, SI $\geq 0$, color scale bar in the Figure. The color plot highlights the increase in SI as a guide to the increased stability of the precipitate. The boundaries of the colored regions represent the stability limit of the mineral species.

shows such a limited behavior as kuramite. Again, a decreasing stability series is observed: stannoidite > chatkalite ~ mawsonite > kesterite ~ stannite ~ petrukite.

It should be noted that four additional phases were considered according to the data in Tables 1 and 2: $Cu_2Sn_3S_7$, $Cu_4Sn_7S_{16}$, mohite ($Cu_2SnS_3$) and rhodostannite ($Cu_2FeSn_3S_8$). All phases were found to be essentially soluble in the calculations carried out. In fact, $Cu_2Sn_3S_7$ and $Cu_4Sn_7S_{16}$ show a stability field even smaller than that of kuramite (Fig. SI14). Conversely, mohite and rhodostannite appear to be completely soluble in the whole pe vs. pH diagram.

### 3.2.1. *Effect of anion concentration on stability boundaries*

Since some of the boundaries of the stability field described above were found to be limited by processes involving the anionic S species, we decided to check the effect of varying the total S concentration in the model system on the stability fields of the phases considered. Indeed, the relative abundance of metals and sulfide/polysulfide species in solution is a parameter relevant to both natural minerogenetic processes and synthetic routes in materials science. Fig. 5a and b shows the stability fields of two selected species, kesterite and $Cu_4Sn_7S_{16}$, as examples of the two main trends observed in the dataset. Similar diagrams for all

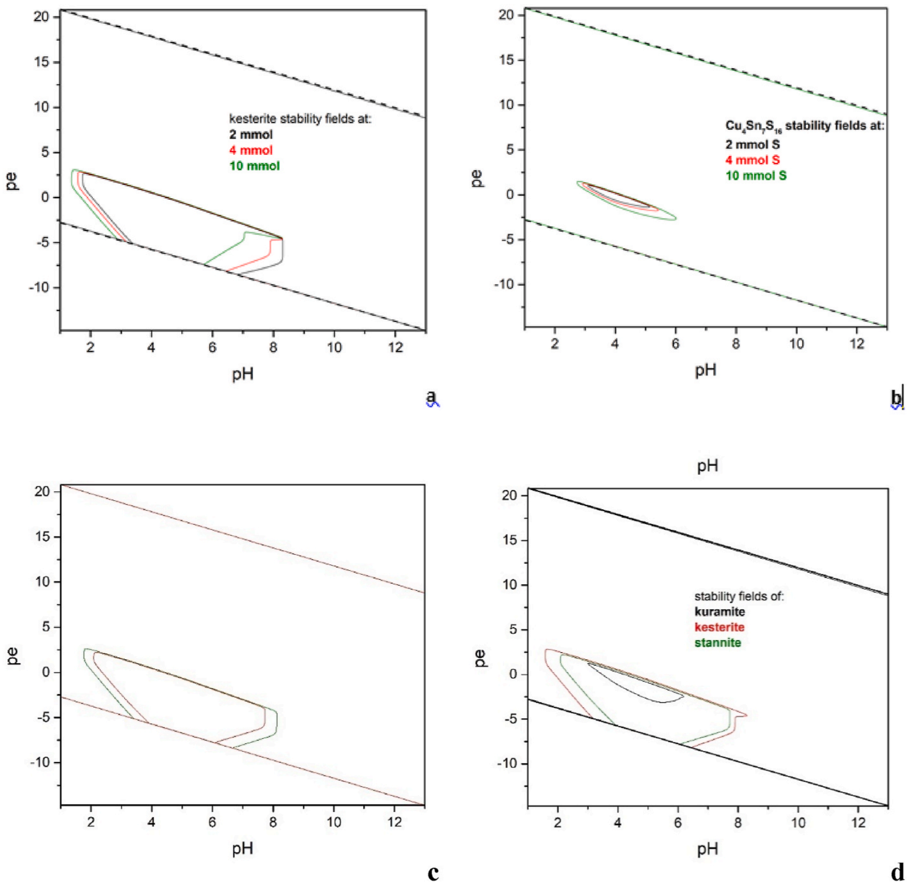

**Fig. 5.** pE versus pH diagrams comparing the stability fields boundaries for selected species: (a) kesterite and (b) $Cu_4Sn_7S_{16}$. The red, black and green continuous lines represent the stability boundary for S concentration set at 2, 4 and $10 \cdot 10^{-3}$ mol/Kgw, respectively. Cu, Zn and Sn are conventionally set at $1 \cdot 10^{-3}$ mol/Kgw. Comparison between stannite, red line, and petrukite, green line (c); Cu, Fe, and Sn are conventionally set at $1 \cdot 10^{-3}$ mol/Kgw, S at $4 \cdot 10^{-3}$ mol/Kgw. Comparison among kuramite, stannite and kesterite, traced by black, green and red lines, respectively (d). Cu, Fe, Zn and Sn are conventionally set at $1 \cdot 10^{-3}$ mol/Kgw, S at $4 \cdot 10^{-3}$ mol/Kgw.

other phases considered in the study are shown in Figure SI15, in the Supporting Information file.

In the pe-pH diagrams of Fig. 5 and SI15, only the boundaries of the stability region calculated at a given S concentration are shown to facilitate comparison with results obtained for the same phase at different S concentrations. As expected, all samples show two distinct and opposite trends, well-illustrated by the phases shown in Fig. 5. $Cu_2Sn_3S_7$, $Cu_4Sn_7S_{16}$ (Fig. 5b) and mohite show an increase in the solid phase stability region with increasing S concentration. In accordance with the Le Chatelier principle, this behavior can be attributed to an increase in one of the ions that contributes to the precipitation of a poorly soluble species in the solution. All the other ternary and quaternary phases considered in the study show a markedly opposite behavior (Fig. 5a): the phase stability region decreases as the total sulfur concentration in the solution increases. This counter-intuitive behavior could be explained by considering the role that sulfide and polysulfide anions, which are stable at low pe and high pH, could play in complexing metal cations (particularly Cu), thus shifting the right boundaries of the stability region towards lower pH values. Specific calculations were carried out to verify the relevance of the above process, and the Cu polysulfide and sulfide complexes (mainly with $HS^-$) resulted in the most abundant Cu- and S- species in solution above 8–10 and 6–8 pH units, respectively, depending on the total S concentration. At the same time, a less pronounced shift of the boundary towards lower pH values is observed in the low pH range. This shift is in accordance with the Le Chatelier principle, as discussed for the phases belonging to the other group. The combined effect of a simultaneous shift towards lower pH values at the left and right of the stability region implies that the stability field exhibits an overall shift towards "acidification" with increasing total sulfur concentration.

The reasons why the considered mineral phases are grouped into two clusters with such different general behavior are due to their different stability behavior. Phases for which the solubility (i.e. $K_{ps}$) is low enough to allow their existence as precipitates even at pH values where the concentration of polysulfide species becomes relevant (i.e. pH > 6) may show the counterintuitive tendency. Phases whose stability field is generally confined in the 2–6 pH window show a Le Chatelier-like tendency.

Finally, a notable exception is rhodostannite, whose stability field was not observed in any of the models developed in the study. This finding, although indicative of a relatively high solubility of this phase in water solution, can be attributed to the fact that this phase, usually obtained by solid state reaction at T > 298 K, could be metastable and therefore not easily described by the present approach. Further work on this subject is in progress. Furthermore, the latter evidence well compares with global instability index (GII) calculations, which give the highest value for rhodostannite along with that for petrukite (see Supporting Information, section GII), thus supporting the metastability of these phases.

### 3.2.2. *Comparison of the stability profiles of selected species*

Looking at the results obtained, none of the phases discussed in this study are among the most relevant sulfides present in the aqueous environment. This consideration can be supported by looking at the prevalence diagram shown in Figure SI16, obtained by plotting the most abundant phases (solid or solute, depending on the conditions) in the pe-pH diagram. The plot was obtained by a point-by-point mass balance calculation using the minteq database, to which all the phases listed in Table 3 were added. Apparently, none of the mineral phases discussed above are present. Accordingly, the existence of minerals from such a list in some natural assemblages, as well as their successful synthesis under laboratory conditions, refer to very specific conditions realized during the formation processes, conditions that are not fully reproduced by our calculations.

Nevertheless, at least two cases of comparison between the stability fields of the phases listed in Tables 1 and 2 are worth considering, as they shed light on the relevance of the results obtained. The first is a comparison between stannite and petrukite (Fig. 5c). Apart from possible compositional variations within a limited range, and the 3D packing of S anions, the structural difference between these two minerals is mainly due to the cation disorder in petrukite, which is not present in stannite. Thus, in our calculation, the different boundaries of the two phases are only due to the additional configurational entropy term used in the definition of the thermodynamic parameters for petrukite. In agreement with theory, the stability field increases in petrukite with respect to stannite. It should be recalled that the possible configurational entropy term of the minerals considered in this study is of the same order of magnitude as the uncertainty in the derivation of the $\log K_{eq}$ by combining structural fragments (as shown in the previous sections). Thus, the difference between the boundaries in Fig. 5c could be used as a graphical tool to illustrate the uncertainty in the boundary definition using the extrapolation method adopted.

The second relevant comparison, shown in Fig. 5d, concerns the so-called "kesterites" (kesterite *sensu strictu*, stannite and kuramite), which are highly regarded in materials science. The diagram clearly shows a different size of stability field with the following order: kesterite > stannite > kuramite. The predominance of kuramite in the product observed in many experimental syntheses using the wet method (Giaccherini et al., 2019, 2020) could be attributed to at least two different factors, the effect of which is additive. Most of the syntheses using homogeneous S generation by decomposition of thioorganic compounds (thiourea, thioacetamide) are carried out under buffered conditions (and the buffers are all in regions close to the stability field of kuramite). Indeed, it can be assumed that the sulfide complexes of Zn and Fe counteract the metal uptake by the Cu–Sn–S precipitate initially formed.

## 4. Concluding remarks

In the present study, we have explored the possibility of extending the range of thermochemical information about multinary phases related to the Cu–Fe–Zn–Sn–S system, relevant for applications in materials science. The proposed method, which consists in an extrapolation based on the sum of the thermodynamics of molecular fragments, has been tested against experimental data for some sulfide minerals and the results are in agreement with a 10% uncertainty.

Using the adopted procedure, we were able to obtain the stability pe-pH Pourbaix diagrams for all the phases considered, which will provide a basis for future considerations about synthesis strategies (at least using a wet method in water solution) and durability issues.

## CRediT authorship contribution statement

**Giordano Montegrossi:** Writing – review & editing, Writing – original draft, Validation, Software, Methodology, Formal analysis, Data curation, Conceptualization. **Federica Meloni:** Writing – review & editing, Data curation. **Andrea Giaccherini:** Writing – review & editing, Writing – original draft, Methodology, Formal analysis, Data curation, Conceptualization. **Alessandro Veneri:** Writing – review & editing, Writing – original draft, Validation. **Matteo Ardit:** Writing – review & editing, Writing – original draft, Validation, Supervision, Methodology, Formal analysis, Data curation, Conceptualization. **Matteo Mannini:** Writing – review & editing, Writing – original draft, Validation. **Francesco Di Benedetto:** Writing – review & editing, Writing – original draft, Visualization, Validation, Supervision, Resources, Methodology, Funding acquisition, Formal analysis, Data curation, Conceptualization.

## Funding sources

FDB acknowledges the funding of this research by Italian MUR, through PRIN 2022 PNRR project P20229723Z (CUP: B53D23025560001), and by Università degli Studi di Ferrara, through the programs FAR2023 and FAR2024.

## Declaration of competing interest

The authors declare the following financial interests/personal relationships which may be considered as potential competing interests: Francesco Di Benedetto reports financial support was provided by University of Ferrara Department of Physics and Earth Sciences. Francesco Di Benedetto reports a relationship with Governement of Italy Ministry of University and Research that includes: funding grants. If there are other authors, they declare that they have no known competing financial interests or personal relationships that could have appeared to influence the work reported in this paper.

## Appendix A. Supplementary data

Supplementary data to this article can be found online at https://doi.org/10.1016/j.apgeochem.2025.106513.

## Data availability

Data will be made available on request.

## References

Allison, J.D., Brown, D.S., Novo-Gradac, K.J., 1991. MINTEQA2/PRODEFA2, a geochemical assessment model for environmental systems: Version 3.0 user's manual.

Aquino, A., et al., 2020. Thermochemical stability of delafossite and other relevant ternary phases in the Cu–Fe–S–O–H system. Appl. Geochem. 123, 104795.

Baláž, P., et al., 2017a. Mechanochemical solvent-free synthesis of Quaternary semiconductor Cu-Fe-Sn-S nanocrystals. Nanoscale Res. Lett. 12, 256.

Baláž, P., et al., 2017b. Chalcogenide Quaternary $Cu_2FeSnS_4$ nanocrystals for solar cells: explosive character of mechanochemical synthesis and environmental challenge. Crystals 7, 367.

Baláž, P., et al., 2019. Mechanochemistry for thermoelectrics: nanobulk $Cu_6Fe_2SnS_8$/$Cu_2FeSnS_4$ composite synthesized in an industrial mill. J. Electron. Mater. 48, 1846–1856.

Baláž, M., et al., 2021a. Scalable and environmentally friendly mechanochemical synthesis of nanocrystalline rhodostannite ($Cu_2FeSn_3S_8$). Powder Technol. 388, 192–200.

Baláž, P., et al., 2021b. Thermoelectric Cu–S-Based materials synthesized via a scalable mechanochemical process. ACS Sustain. Chem. Eng. 9, 2003–2016.

Belmonte, D., Ottonello, G., Zuccolini, M.V., 2014. Ab initio thermodynamic and thermophysical properties of sapphirine end-members in the join $Mg_4Al_8Si_2O_{20}$-$Mg_3Al_{10}SiO_{20}$. Am. Mineral. 99, 1449–1461.

Baláž, M., et al., 2024. Mechanochemical preparation of nanocrystalline Stannite/Chatkalite composite: kinetics of synthesis and thermoelectric properties. J. Therm. Anal. Calorim. 149, 10393–10404.

Belmonte, D., et al., 2016. Ab initio thermodynamic and thermophysical properties of sodium metasilicate, $Na_2SiO_3$, and their electron-density and electron-pair-density counterparts. J. Phys. Chem. A 120, 8881–8895.

Belmonte, D., La Fortezza, M., Menescardi, F., 2022. Ab initio thermal expansion and thermoelastic properties of ringwoodite ($\gamma$-$Mg_2SiO_4$) at mantle transition zone conditions. Eur. J. Mineral. 34, 167–182.

Blanc, P., 2008. Thermoddem : sélection de propriétés thermodynamiques pour les principales espèces aqueuses et minérales porteuses de fer. BRGMRP-56587-FR Open Rep. 73p. https://thermoddem.brgm.fr/sites/default/files/upload/documents/blanc-2008-brgm-rp-56587-fr.pdf.

Blanc, Ph, et al., 2012. Thermoddem: a geochemical database focused on low temperature water/rock interactions and waste materials. Appl. Geochem. 27, 2107–2116.

Bonazzi, P., et al., 2003. A model for the mechanism of incorporation of Cu, Fe and Zn in the stannite - kërsterite series, $Cu_2FeSnS_4$ -. Cu2ZnSnS4. Can. Mineral. 41, 639–647.

Chen, X., et al., 1998. Synthesis, electrical conductivity, and crystal structure of $Cu_4Sn_7S_{16}$ and structure refinement of $Cu_2SnS_3$. J. Solid State Chem. 139, 144–151.

Chen, X. -a, Wada, H., Sato, A., 1999. Preparation, crystal structure and electrical properties of $Cu_4SnS_6$. Mater. Res. Bull. 34, 239–247.

Chong, W., et al., 2022. Insights from density functional theory calculations on heteroatom P-doped $ZnIn_2S_4$ bilayer nanosheets with atomic-level charge steering for photocatalytic water splitting. Sci. Rep. 12, 1927.

Choudhury, A., et al., 2017. New insights into the structure, chemistry, and properties of $Cu_4SnS_4$. J. Solid State Chem. 253, 192–201.

Delany, J.M., Lundeen, S.R., 1991. The LLNL Thermochemical Data Base – Revised Data and File Format for the EQ3/6 Package.

Di Benedetto, F., et al., 2006. First evidence of natural superconductivity: covellite. Eur. J. Mineral. 18, 283–287.

Digraskar, R.V., et al., 2019. CZTS decorated on graphene oxide as an efficient electrocatalyst for high-performance hydrogen evolution reaction. ACS Omega 4, 7650–7657.

Evans, H.T., 1979. The crystal structures of low chalcocite and djurIeite. Z. Krist. 150, 299–320.

Giaccherini, A., Montegrossi, G., Di Benedetto, F., 2016. Stability of naturally relevant ternary phases in the Cu–Sn–S System in contact with an aqueous solution. Minerals 6, 79.

Fleischer, M., et al., 1982. New mineral names. Am. Mineral. 67, 621–624.

Giaccherini, A., et al., 2019. Green and scalable synthesis of nanocrystalline kuramite. Beilstein J. Nanotechnol. 10, 2073–2083.

Giaccherini, A., et al., 2020. A new solvothermal approach to obtain nanoparticles in the $Cu_3SnS_4$-$Cu_2FeSnS_4$ join. J. Geosci. 65, 3–14.

Goto, Y., et al., 2013. Enhanced thermoelectric figure of merit in Stannite–Kuramite solid solutions $Cu_{2+x}Fe_{1-x}SnS_{4-y}$ ($x = 0$–1) with anisotropy lowering. Inorg. Chem. 52, 9861–9866.

Gürel, T., Sevik, C., Çağın, T., 2011. Characterization of vibrational and mechanical properties of quaternary compounds $Cu_2ZnSnS_4$and $Cu_2ZnSnSe_4$in kesterite and stannite structures. Phys. Rev. B 84.

Hall, S.R., Szymasky, J.T., Stewart, J.M., 1978. Kesterite, $Cu_2(Zn,Fe)SnS_4$, and Stannite, $Cu_2(FeZn)SnS_4$, structurally similar but distinct minerals. Can. Mineral. 16, 131–137.

Helgeson, H.C., et al., 1978. Summary and critique of the thermodynamic properties of rock-forming minerals. Am. J. Sci. 278-A, 1–129.

Helgeson, H.C., Kirkham, D.H., Flowers, G.C., 1981. Theoretical prediction of the thermodynamic behavior of aqueous electrolytes at high pressures and temperatures: IV. Calculation of activity coefficients, osmotic coefficients, and apparent molal and standard and relative partial molal properties to 600°C and 5kb. Am. J. Sci. 281, 1249–1516.

Huang, H.-H., 2016. The Eh-pH diagram and its advances. Metals 6, 23.

Jaulmes, S., Rivet, J., Laruelle, P., 1977. Cuivre-Etain-Soufre $Cu_4SnS_4$. Acta Crystallogr. Sect. B Struct. Sci. Cryst. Eng. Mater. 33, 540–542.

Johnson, J.W., Oelkers, E.H., Helgeson, H.C., 1992. SUPCRT92: a software package for calculating the standard molal thermodynamic properties of minerals, gases, aqueous species, and reactions from 1 to 5000 bar and 0 to 1000°C. Comput. Geosci. 18, 899–947.

Jumas, J.C., Philippot, E., Maurin, M., 1979. Structure du Rhodostannite Synthétique. Acta Crystallogr. Sect. B Struct. Sci. Cryst. Eng. Mater. 35, 2195–2197.

Kissin, S.A., Owens, D.A.R., 1989. The relatives of stannite in the light of new data. Can. Mineral. 27, 673–688.

Kondepudi, D.K., Prigogine, I., 1998. Modern Thermodynamics: from Heat Engines to Dissipative Structures. John Wiley & Sons Inc.

Kovalenker, V.A., 1981. Kuramite, $Cu_3SnS_4$, a new mineral of the stannite group. Int. Geol. Rev. 23, 365–370.

Kovalenker, V.A., 1983. Mohite, $Cu_2SnS_3$, a new sulfide of tin and copper. Int. Geol. Rev. 25, 117–120.

Kudoh, Y., Takeuchi, Y., 1976. The superstructure of stannoidite. Z. Krist 144, 145–160.

Kumar, V.P., et al., 2021. Local-Disorder-Induced low thermal conductivity in degenerate semiconductor $Cu_{22}Sn_{10}S_{32}$. Inorg. Chem. 60, 16273–16285.

Lohani, K., et al., 2020. Ultra-low thermal conductivity and improved thermoelectric performance in disordered nanostructured copper tin sulphide ($Cu_2SnS_3$, CTS). J. Alloys Compd. 830, 154604.

Markham, N., Lawrence, L., 1965. Mawsonite, a new cpper-iron-tin sulfide from Mt. Lyell, Tasmania and Tynhga, New South wales. Am. Mineral. 50, 900–908.

Meng, X., et al., 2015. Sulfurization temperature dependence of the structural transition in $Cu_2FeSnS_4$-based thin films. Mater. Lett. 161, 427–430.

Mighell, Alan D., 2006. Ambiguities in powder indexing: the impact of a Quaternary lattice metric singularity on the characterization of mawsonite and chatkalite. J. Res. Natl. Inst. Stand. Technol. 111, 393–399.

Moëlo, Y., et al., 2008. Sulfosalt systematics: a review. Report of the sulfosalt sub-committee of the IMA Commission on Ore Mineralogy. Eur. J. Mineral 20, 7–62.

Momma, K., Izumi, F., 2011. *VESTA3* for three-dimensional visualization of crystal, volumetric and morphology data. J. Appl. Crystallogr. 44, 1272–1276.

Ohmasa, M., Suzuki, M., Takeuchi, Y., 1977. A refinement of the crystal structure of covellite, CuS. Mineral. J. 8, 311–319.

Olatunde, O.C., Onwudiwe, D.C., 2022. Selective syntheses of kuramite ($Cu_2SnS_3$) and petrukite ($Cu_3SnS_4$) phases of copper tin sulphide, and their electrochemical and photocatalytic properties. Results Mater. 13, 100249.

Onoda, M., et al., 2000. Crystal structure and twinning of monoclinic $Cu_2SnS_3$. Mater. Res. Bull. 35, 1563–1570.

Parkhurst, Appelo, C.A.J., 1999. User's guide to PHREEQC (Version 2): a Computer Program for speciation, Batch-Reaction, one-dimensional transport, and inverse geochemical calculations. http://pubs.er.usgs.gov/publication/wri994259.

Pavan Kumar, V., et al., 2017. Copper Hyper-Stoichiometry: the Key for the Optimization of Thermoelectric Properties in Stannoidite $Cu_{8+x}Fe_{3-x}Sn_2S_{12}$. J. Phys. Chem. C 121, 16454–16461.

Pavan Kumar, V., et al., 2021. Ordered sphalerite derivative $Cu_5Sn_2S_7$: a degenerate semiconductor with high carrier mobility in the Cu–Sn–S diagram. J. Mater. Chem. A 9, 10812–10826.

Robie, R.A., Hemingway, B.S., 1995. Thermodynamic Properties of Minerals and Related Substances at 298.15 K and 1 bar (105 Pascals) Pressure and at Higher Temperatures. USGS.

Schorr, S., 2007. Structural aspects of adamantine like multinary chalcogenides. Thin Solid Films 515, 5985–5991.

Schorr, S., Hoebler, H.-J., Tovar, M., 2007. A neutron diffraction study of the stannite-kesterite solid solution series. Eur. J. Mineral 19, 65–73.

Siloi, I., et al., 2019. Thermoelectric properties of minerals with the mawsonite structure. ACS Appl. Energy Mater. 2, 8068–8078.

Skinner, B.J., Erd, R.C., Grimaldi, F.S., 1964. Greigite the thiospinel of Fe: a new mineral. Am. Mineral. 49, 543–555.

Springer, G., 1968. Electronprobe analyses of stannite and related tin minerals. Mineral. Mag. J. Mineral Soc. 36, 1045–1051.

Stolyarova, T.A., Baranov, A.V., Osadchii, E.G., 2018. Calorimetric determination of the standard enthalpy of formation of stannite, $Cu_2FeSnS_4$. Geochem. Int. 56, 75–77.

Stolyarova, T.A., Osadchii, E.G., Baranov, A.V., 2019. Standard enthalpy of kesterite ($Cu_2ZnSnS_4$) formation. Geochem. Int. 57, 109–111.

Subramani, T., et al., 2020. Greigite ($Fe_3S_4$) is thermodynamically stable: implications for its terrestrial and planetary occurrence. Proc. Natl. Acad. Sci. 117, 28645–28648.

Szymanski, J.T., 1976. The crystal structure of mawsonite, $Cu_6Fe_2SnS_8$. Can. Mineral. 14, 529–535.

Tardy, Y., 1976. Prediction of Gibbs energies of formation-4 relationships among Gibbs energies of formation of hydroxides, oxides and aqueous ions. Geochem. Cosmochim. Acta 40, 1051–1056.

Tardy, Y., Garrels, K.M., 1974. A method of estimating the Gibbs energies of formation of layer silicates. Geochem. Cosmochim. Acta 38, 1101–1116.

Tardy, Y., Vieillard, P., 1977. Relationships among Gibbs free energies and enthalpies of formation of phosphates, oxides and aqueous ions. Contrib. Mineral. Petrol. 63, 75–88.

University of Oregon, 2015. SOLTHERM Thermodynamic Database for Geochemical Modeling.

Wang, N., 1974. The three ternary phases in the system Cu-Sn-S. Neues Jahrbuch Mineral. Monatsh. 424–431, 1974.

Wang, N., 1976. Idaite and the synthetic phases $Cu_{4.33}Ge_{0.67}S_5$ and $Cu_{9.67}Sn_{2.33}S_{13}$. Neues Jahrbuch Mineral. Monatsh. 241–247, 1976.

Wang, A., et al., 2023. A critical review on the progress of kesterite solar cells: current strategies and insights. Adv. Energy Mater. 13, 2203046.

webmineral.com, 2024. Dana Sulfide Classification.

Wu, D., Knowles, C.R., Chang, L.L.Y., 1986. Copper-tin sulphides in the system Cu-Sn-S. Mineral. Mag. 50, 323–325.

Wu, C., et al., 2007. Hexagonal $Cu_2SnS_3$ with metallic character: another category of conducting sulfides. Appl. Phys. Lett. 91, 143104.

Yamanaka, T., Kato, A., 1976. Moessbauer effect study of $^{57}$Fe and $^{119}$Sn in stannite, stannoidite, and mawsonite. Am. Mineral. 61, 260–265.

Zalewski, W., et al., 2010. XAFS study of kesterite, kuramite and stannite type alloys. J. Alloys Compd. 492, 35–38.